Original article

JSA

J Strain Analysis
2016, Vol. 51(6) 431–443

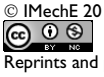

DOI: 10.1177/0309324716649529
sdj.sagepub.com


First-order correction to counter the effect of eccentricity on the hole-drilling integral method with strain-gage rosettes

Michele Barsanti, Marco Beghini, Leonardo Bertini, Bernardo D Monelli and Ciro Santus

Abstract

The offset between the hole and the centre of the strain-gage rosette is unavoidable, although usually small, in the hole-drilling technique for residual stress evaluation. In this article, we revised the integral method described in the ASTM E837 standard and we recalculated the calibration coefficients. The integral method was then extended by taking into account the two eccentricity components, and a more general procedure was proposed including the first-order correction. A numerical validation analysis was used to consolidate the procedure and evaluate the residual error after implementing the correction. The values of this error resulted limited to a few percentage points, even for eccentricities larger than the usual experimental values. The narrow eccentricity limit claimed by the standard, to keep the maximum error lower than 10%, can now be considered extended by approximately a factor of 10, after implementing the proposed correcting procedure, proving that the effect of the eccentricity is mainly linear within a relatively large range.

Keywords

Residual stresses, hole-drilling method, integral method, eccentricity correction, finite element analysis

Date received: 8 January 2016; accepted: 12 April 2016

Introduction

Residual stresses can significantly influence the strength of mechanical components, especially under cyclic fatigue loading.[1] There are several experimental techniques for measuring residual stresses.[2] These include mechanical methods (destructive or semi-destructive) based on cuttings or local material removals to relieve the embedded residual stresses, such as the contour method,[3] the ring core method[4–6] and other specific approaches adapted to the geometry of the components investigated,[7–11] or also combining the hole-drilling method with the indentation.[12] After the material has been removed, a back calculation is required to obtain the residual stress distribution that has been relaxed.[13,14] The hole-drilling method is the most popular and widely investigated.[15,16] Its hardware is easily implemented, it is relatively inexpensive and it directly provides the stresses at a point; specifically, it averages the stress on the small volume of the removed material. Hole-drilling can be performed by measuring the entire field of the relaxed deformation with optical methods[17] both on the isotropic elastic materials, namely, steel or other metallic alloys, and on the orthotropic materials such as composite plates.[18] However, the hole-drilling technique is usually performed just with a strain-gage rosette to measure the relaxed strains in the near area of the drilled hole. There are many application examples of this technique such as large components showing a flat (or almost flat) surface,[19] deep rolled or shot peened flat specimens,[20,21] and recently even on coated surfaces.[22–25] The usual rosette for hole-drilling has three grids angularly placed at 0°, 225°, 90°. Alternatively, the 0°, 45°, 90° grid pattern can be used without making any difference, for the angular periodicity of the stresses, unless a hole eccentricity is introduced. Figure 1 shows the hole-drilling set-up with type A or type B three grid rosettes according to the American Society for Testing

Department of Civil and Industrial Engineering (DICI), University of Pisa, Italy

Corresponding author:
Ciro Santus, Department of Civil and Industrial Engineering (DICI), University of Pisa, Largo L. Lazzarino 2, 56122 Pisa, Italy.
Email: ciro.santus@ing.unipi.it

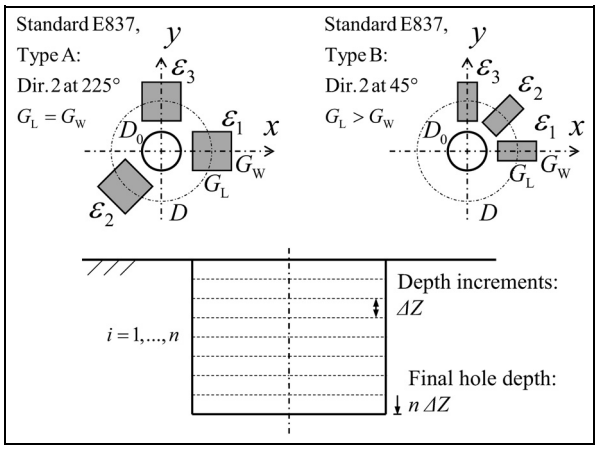

Figure 1. Hole-drilling method with type A and type B rosettes according to the CCW numbering system.

and Materials (ASTM) standard. Besides the direction 2 at 45°, rather than at 225°, type B has a smaller grid width than grid length to prevent any geometry interference.

After having measured and recorded the relaxed strains, the *integral method* is usually considered for the calculation of the residual stress distributions. The integral method was initially proposed by Schajer[26,27] and recently has been widely used and also conformed to specific cases, such as medium thick plates[28] and thin plates,[29] as well as being extended to optical methods.[30] The ASTM E837-13a standard[31] codifies the hole-drilling integral method, with a strain-gage rosette. The calculation proposed takes into account that a variable distribution can be obtained, where the stresses are assumed to be piecewise constant over each hole depth increment. Then, the standard reports the calibration coefficients (dimensionless and in matrix format) which depend only on the geometry, thus enabling the residual stresses from the measured relaxed strains to be calculated.

Error analysis is crucial for any residual stress experimental technique; indeed, we recently proposed a bending test rig for providing a validation concurrently with the measure itself.[32,33] Many investigations can be cited from the literature considering different sources of errors for the hole-drilling technique. The strain measure uncertainty, which is the most important,[34] can be reduced to some extent by following the regularization procedure proposed by Schajer[35] and then implemented in the ASTM E837 starting from the 2008 issue. Another source of error affecting the hole-drilling measures is the plasticity induced by the drilling, for which we proposed a correction in a previous study.[36,37] The shape, radius and the position of the hole are also the reasons for experimental uncertainty. The flatness of the bottom surface was questioned by Scafidi et al.[38] and then by Nau and Scholtes,[39] while the problem of eccentricity was initially investigated analytically by Ajovalasit[40] for a thin workpiece where a through-hole (plane stress) assumption can be used. More recently, Beghini et al.[41,42] introduced the influence function approach, for a blind hole in a thick workpiece. The strain field was computed starting from a database of numerical solutions, implementing a specific geometric configuration in which the components of eccentricity are merely introduced as the geometry parameters rather than being considered as a source of error. The integral method according to the ASTM E837 standard enables the residual stress calculation to be easily implemented, but the presence of hole eccentricity is a limitation. The standard requires a nearly perfect concentricity between the hole and the rosette. The prescribed maximum allowable eccentricity value is $0.004\,D$ so that the maximum eccentricity is 0.02 mm for the usual rosettes with $D = 5.13$ mm. The current positioning accuracy is usually in the order of a few hundredths of millimetres; thus, the eccentricity values are sometimes higher than this standard limitation. The numerical simulations, as reported below, showed that an eccentricity in the order of these values can introduce some percentage points of error on the residual stress components. In order to improve the integral method, this article proposes a correction procedure based on the first-order linearization of the calibration matrices, which considerably extends the tolerable eccentricity.

Integral method

Within the concentricity assumption, the axial-symmetric geometry allows a decoupling between the components of stress with respect to the corresponding relaxed strains. The residual stresses are related to the relaxed strains according to the general relationship introduced by Schajer[26,27]

$$\varepsilon_r(\vartheta) = A(\sigma_{max} + \sigma_{min}) + B(\sigma_{max} - \sigma_{min})\cos(2\vartheta) \tag{1}$$

where σ_{max} and σ_{min} are the principal residual stresses, ϑ is the angle of the generic rosette grid with respect to the direction of σ_{max} and A and B are the two elastic constants. After introducing a three-grid rosette with a generic orientation with respect to the principal directions, the following matrix equation holds

$$\begin{bmatrix} (A+B) & (A-B) & 0 \\ A & A & 2B \\ (A-B) & (A+B) & 0 \end{bmatrix} \begin{bmatrix} \sigma_x \\ \sigma_y \\ \tau_{xy} \end{bmatrix} = \begin{bmatrix} \varepsilon_1 \\ \varepsilon_2 \\ \varepsilon_3 \end{bmatrix} \tag{2}$$

in which 1, 2 and 3 are the three grid directions: 0°, 225°, 90° or 0°, 45°, 90°. Given that directions 1 and 3 are orthogonal and numbered as counter-clockwise (CCW), a reference system for the problem is inherently introduced, and the axes x and y for the residual stress components can be oriented according to the directions 1 and 3, respectively (Figure 1). Alternatively, a clockwise (CW) orientation could be introduced (in agreement with the ASTM E837 standard); however, the orientation of grid 3 would be opposite to the direction

of the y-axis. The form of equation (2) suggests combining the variables according to an equibiaxial stress, and the related strain, plus two components of pure shear stress and the relative strains

$$\begin{aligned} P &= \frac{(\sigma_y + \sigma_x)}{2}, Q = \frac{(\sigma_y - \sigma_x)}{2}, T = \tau_{xy} \\ p &= \frac{(\varepsilon_3 + \varepsilon_1)}{2}, q = \frac{(\varepsilon_3 - \varepsilon_1)}{2}, \\ t &= \frac{2\varepsilon_2 - (\varepsilon_3 + \varepsilon_1)}{2} = \varepsilon_2 - p \end{aligned} \tag{3}$$

In the second of equation (3), the component of strain t has been intentionally defined with the opposite sign with respect to the ASTM standard in order to have sign consistency between the shear stress τ_{xy} and the relaxed strain ε_2. For example, when the equibiaxial stress component P is positive, then the strain p is negative; indeed, the coefficients A and B are both negative since the measured strains are the *relaxed* deformations. Similarly, when a positive shear stress τ_{xy} is introduced, the principal stress along the 45° angle is tensile; therefore, ε_2 turns out to be negative and thus t also has to be negative. Having the grid direction 2 at 225° makes no difference and the last of equation (3) is still valid. The opposite definition for the t strain component would be consistent for a CCW rosette with the grid 2 direction at 135°, or alternatively at −45°. However, this is never the case for the type of rosettes usually available, although the possible use of this scheme is mentioned by Nau and Scholtes.[39] On the other hand, introducing the CW grid numbering system as shown in the ASTM standard, the second grid is either in the second quadrant (type A) or in the fourth quadrant (type B), and consequently, the opposite definition for t is correct, as reported in the standard. The numbering system CCW was considered preferential for this study since it simplifies the sign definition of the eccentricity components with both the two orthogonal grids 1 and 3 oriented along the positive sign of the x- and y-axes. After substituting the definitions of equation (3) into equation (2), the three variables are decoupled; thus, the matrix relating stresses and strains are diagonal containing the two coefficients A and B

$$\begin{bmatrix} 2A & 0 & 0 \\ 0 & 2B & 0 \\ 0 & 0 & 2B \end{bmatrix} \begin{bmatrix} P \\ Q \\ T \end{bmatrix} = \begin{bmatrix} p \\ q \\ t \end{bmatrix} \tag{4}$$

This linear dependence between the residual stresses and the relaxed strains is a consequence of the elasticity behaviour of the material. Therefore, equation (4) can be rewritten with the explicit dependence of Young's modulus E and also the negative sign of the two coefficients can be emphasized

$$-\frac{1}{E}\begin{bmatrix} \alpha & 0 & 0 \\ 0 & \beta & 0 \\ 0 & 0 & \beta \end{bmatrix} \begin{bmatrix} P \\ Q \\ T \end{bmatrix} = \begin{bmatrix} p \\ q \\ t \end{bmatrix} \tag{5}$$

where α and β depend on the Poisson's ratio ν and on the ratios between the hole and the rosette dimensions, but they do not depend on Young's modulus.

The stress–strain relation of equation (5) only considers a single value of the stress state, which is assumed to be uniform along the depth. In the specific case of small thickness, plane stress, this relationship can be further developed by making explicit the dependence on the Poisson's ratio ν which only applies on the equibiaxial stress component, thus obtaining equation (6)

$$-\frac{1}{E}\begin{bmatrix} a(1+\nu) & 0 & 0 \\ 0 & b & 0 \\ 0 & 0 & b \end{bmatrix} \begin{bmatrix} P \\ Q \\ T \end{bmatrix} = \begin{bmatrix} p \\ q \\ t \end{bmatrix} \tag{6}$$

where, according to equation (5), $\alpha = a(1+\nu), \beta = b$. Now the coefficients a and b are scalar, positive, dimensionless and only depend on the geometry ratios, while they do not depend on the size. When the method is applied to a surface of a bulk component (blind hole), and the state of stress can be assumed to be uniform up to the final depth of the hole, the dependence on the Poisson's ratio according to equation (6) only has an approximate validity. However, this effect can be neglected, since it produces a perturbation of the values in the order of a few percentage points, as discussed below. Thus, the dependency on ν can also be kept for the blind hole problem, as proposed in equation (6) which tolerates some inaccuracy; otherwise, a recalculation of the coefficients is required for any value of ν.

A major development of the method is the introduction of a possible non-uniform distribution, in which the components of stress are introduced as uniform stepwise. There are thus three independent components for each increment of the hole. In this case, the scalars p, q, t and P, Q, T are replaced with vectors and the coefficients a, b are replaced with the calibration coefficient matrices

$$-\frac{1+\nu}{E}\bar{\mathbf{a}}\mathbf{P} = \mathbf{p}, \; -\frac{1}{E}\bar{\mathbf{b}}\mathbf{Q} = \mathbf{q}, \; -\frac{1}{E}\bar{\mathbf{b}}\mathbf{T} = \mathbf{t} \tag{7}$$

Vectors $\mathbf{P} = (P^{(1)}, P^{(2)}, \ldots, P^{(n)})^{\mathrm{T}}, \mathbf{Q}, \mathbf{T}$ and similarly $\mathbf{p} = (p^{(1)}, p^{(2)}, \ldots, p^{(n)})^{\mathrm{T}}, \mathbf{q}, \mathbf{t}$ represent the stresses and strains following the logic of decoupling, introduced previously, and $i = 1, 2, \ldots n$ are the depth positions along the increments of the hole. The matrices $\bar{\mathbf{a}}$ and $\bar{\mathbf{b}}$ are lower triangular since the residual stress of the material removed in the previous steps has a (linear) cumulative effect on the relaxed strains, while the residual stress of the material below, which still has to be removed, has no effect on the relaxed strains. Therefore, the coefficients a_{ij} and b_{ij} of the matrices $\bar{\mathbf{a}}$ and $\bar{\mathbf{b}}$ are all positive for $i \geqslant j$, while they are 0 for $i < j$. For example, just with three drilling steps, the coefficient matrices are

$$\bar{\mathbf{a}} = \begin{bmatrix} a_{11} & 0 & 0 \\ a_{21} & a_{22} & 0 \\ a_{31} & a_{32} & a_{33} \end{bmatrix}, \bar{\mathbf{b}} = \begin{bmatrix} b_{11} & 0 & 0 \\ b_{21} & b_{22} & 0 \\ b_{31} & b_{32} & b_{33} \end{bmatrix} \tag{8}$$

The integral method with variable stress distribution, which is summarized in equation (7), just requires the axial symmetry of the removed material shape and the orientation of the measurement grids according to the $0°, 225°(45°), 90°$ scheme. Thus, the method can be extended to different problems that share these geometric characteristics, such as the ring core method where material removal is annular and the grids are superimposed on the central volume according to the same angular pattern.

Extension of the integral method to the eccentricity

When an eccentricity between the drilled hole and the rosette is introduced, even if small, equation (1) is no longer valid. Therefore, it is not possible to decouple the p, q, t components and a new formulation is required. By following a more general approach, a linear relationship between all the components of stress and strain can still be proposed, equation (9)

$$-\frac{1}{E}\bar{\mathbf{A}}\mathbf{S} = \mathbf{e} \tag{9}$$

where $\mathbf{S} = (\sigma_x^{(1)}, \sigma_y^{(1)}, \tau_{xy}^{(1)}, \ldots, \sigma_x^{(n)}, \sigma_y^{(n)}, \tau_{xy}^{(n)})^{\mathrm{T}}$ is the vector of all the components of residual stresses, collected in blocks of three terms, for different values of depth, and similarly $\mathbf{e} = (\varepsilon_1^{(1)}, \varepsilon_2^{(1)}, \varepsilon_3^{(1)}, \ldots, \varepsilon_1^{(n)}, \varepsilon_2^{(n)}, \varepsilon_3^{(n)})^{\mathrm{T}}$ is the vector of the relaxed strains. Since the three components of stresses and strains are arranged in blocks, $\bar{\mathbf{A}}$ is a lower triangular 3×3 block matrix. An example with three depth increments is reported below

$$\bar{\mathbf{A}} = \left[\begin{array}{ccc|ccc|ccc}
A_{11}^{(11)} & A_{12}^{(11)} & A_{13}^{(11)} & 0 & 0 & 0 & 0 & 0 & 0 \\
A_{21}^{(11)} & A_{22}^{(11)} & A_{23}^{(11)} & 0 & 0 & 0 & 0 & 0 & 0 \\
A^{(11)} & A^{(11)} & A^{(11)} & 0 & 0 & 0 & 0 & 0 & 0 \\
\hline
A_{11}^{(21)} & A_{12}^{(21)} & A_{13}^{(21)} & A^{(22)} & A^{(22)} & A^{(22)} & 0 & 0 & 0 \\
A_{21}^{(21)} & A_{22}^{(21)} & A_{23}^{(21)} & A^{(22)} & A^{(22)} & A^{(22)} & 0 & 0 & 0 \\
A_{31}^{(21)} & A_{32}^{(21)} & A_{33}^{(21)} & A^{(22)} & A^{(22)} & A^{(22)} & 0 & 0 & 0 \\
\hline
A_{11}^{(31)} & A_{12}^{(31)} & A_{13}^{(31)} & A^{(32)} & A^{(32)} & A^{(32)} & A^{(33)} & A^{(33)} & A^{(33)} \\
A_{21}^{(31)} & A_{22}^{(31)} & A_{23}^{(31)} & A^{(32)} & A^{(32)} & A^{(32)} & A^{(33)} & A^{(33)} & A^{(33)} \\
A_{31}^{(31)} & A_{32}^{(31)} & A_{33}^{(31)} & A^{(32)} & A^{(32)} & A^{(32)} & A^{(33)} & A^{(33)} & A^{(33)}
\end{array}\right] \tag{10}$$

The coefficients $A_{hk}^{(ij)}$ have the indexes: $h, k = 1, 2, 3$ and $i = 1, \ldots, n, j = 1, \ldots, i$ where, similarly to above, n is the total number of drilling steps. Again these coefficients do not depend on Young's modulus, but do dependent on the Poisson's ratio, and also on the geometry ratios. More specifically, each of these coefficients also depends on the eccentricity. Therefore, the power series expansion can be applied in terms of the two eccentricity components along directions 1 and 3

$$A_{hk}^{(ij)} = A_{0,hk}^{(ij)} + \frac{\partial}{\partial e_1}A_{hk}^{(ij)}e_1 + \frac{\partial}{\partial e_3}A_{hk}^{(ij)}e_3 + \frac{1}{2}\frac{\partial^2}{\partial e_1^2}A_{hk}^{(ij)}e_1^2 + \frac{1}{2}\frac{\partial^2}{\partial e_3^2}A_{hk}^{(ij)}e_3^2 + \frac{\partial^2}{\partial e_1 \partial e_3}A_{hk}^{(ij)}e_1e_3 + \cdots \tag{11}$$

In equation (11), the two eccentricity components e_1 and e_3 are introduced. Their definition intended here is the offset of the hole with respect to the rosette, which is positive according to the x,y-axes. Provided that x is rightwards and y upwards (Figure 1), when the hole centre is right-shifted, with respect to the grid centre, e_1 is positive; similarly, e_3 is positive when the hole centre is up-shifted. The opposite definition of the eccentricity components, or the use of the CW numbering system, would be equally possible but involving a revision of the derivative coefficient signs. As expected, and confirmed by the numerical analysis reported below, the higher order contributions are negligible, especially for relatively small eccentricity values; thus, it suffices to focus only on the first two linear terms. Furthermore, as matrix $\bar{\mathbf{A}}$ is dimensionless, the derivative terms can also be put in a dimensionless form just by multiplying by a characteristic length of the problem, for example, the average diameter D of the strain-gage rosette, equation (12)

$$A_{hk}^{(ij)} = A_{0,hk}^{(ij)} + \alpha_{1,hk}^{(ij)}\eta_1 + \alpha_{3,hk}^{(ij)}\eta_3 \tag{12}$$

where the dimensionless derivative coefficients and the eccentricity components are

$$\begin{aligned}
\alpha_{1,hk}^{(ij)} &= D\frac{\partial}{\partial e_1}A_{hk}^{(ij)}, \eta_1 = \frac{e_1}{D} \\
\alpha_{3,hk}^{(ij)} &= D\frac{\partial}{\partial e_3}A_{hk}^{(ij)}, \eta_3 = \frac{e_3}{D}
\end{aligned} \tag{13}$$

The coefficients $A_{0,hk}^{(ij)}, \alpha_{1,hk}^{(ij)}, \alpha_{3,hk}^{(ij)}$ can be collected into block triangular matrices

$$\bar{\mathbf{A}}_0 = [A_{0,hk}^{(ij)}], \bar{\alpha}_{\mathrm{e}1} = [\alpha_{1,hk}^{(ij)}], \bar{\alpha}_{\mathrm{e}3} = [\alpha_{3,hk}^{(ij)}] \tag{14}$$

and finally, matrix $\bar{\mathbf{A}}$ can be reconstructed, and approximated to the first order, as

$$\bar{\mathbf{A}} = \bar{\mathbf{A}}_0 + \bar{\alpha}_{\mathrm{e}1}\eta_1 + \bar{\alpha}_{\mathrm{e}3}\eta_3 \tag{15}$$

Clearly, the availability of matrix $\bar{\mathbf{A}}$ allows to solve the *inverse* problem, that is, to determine the profile of the residual stresses from the measured relaxed strains, just by calculating the inverse matrix. Given the rather low size of the matrix, the inversion of $\bar{\mathbf{A}}$ does not involve numerical difficulties and the stress components $\mathbf{S}$ can be easily obtained from the measured strains $\mathbf{e}$

$$\mathbf{S} = -E\bar{\mathbf{A}}^{-1}\mathbf{e} \tag{16}$$

Being the stress component decoupling not used, a three-grid rosette with $0°, 225°(45°), 90°$ pattern is no longer strictly required. A different angular pattern could be proposed or even a higher number of grids could be considered to increase the strain-gage sensitivity. For example, with four grids instead of just three, the matrix would be 4×3 block and the inverse problem solved with the pseudoinverse matrix rather than the square inverse. An example of a rosette with four grids is type D reported by Schajer,[15] which has a

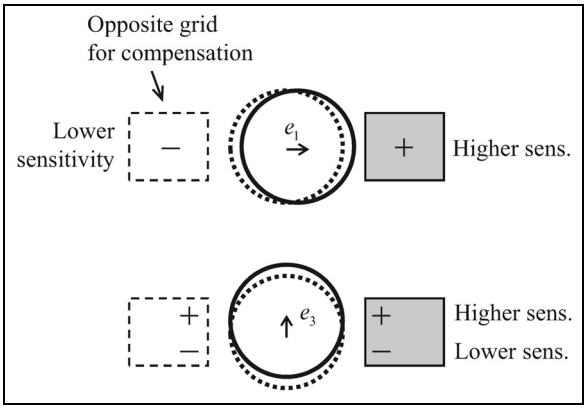

Figure 2. Grid sensitivity to longitudinal and transversal eccentricity components.

specific applicability when a correction of the plasticity effect is required.[36]

Symmetry properties

As shown in Figure 2, the hole eccentricity affects the sensitivity of the grids. When the eccentricity is along the direction of the grid, the sensitivity is higher if the hole is closer to the grid; thus, the absolute value of the measured relaxed strain is larger. On the other hand, if the eccentricity displacement is transversal, a portion of the grid has a higher sensitivity, while the other side has a lower sensitivity and this implies, for symmetry, that the first-order derivative is 0. In fact, some of the coefficients of the matrices $\bar{\alpha}_{e1}, \bar{\alpha}_{e3}$ turn out to be null. If an opposite grid is placed at the other side of the hole and connected in series (Figure 2), another feature of symmetry is introduced. Consequently, even the eccentricity first-order sensitivity along the grid direction is reduced to 0, and the derivative matrices are both entirely null. This situation is clearly of interest. In fact, the first order is systematically cancelled, and procedure p, q, t can be followed without any notable effect caused by the eccentricity. A commercially available rosette of six grids (two grids for each of the three directions) was tested by Beghini et al.[43] and the reduced sensitivity to the eccentricity was experimentally verified. However, introducing another grid for each measurement direction makes the rosette more complicated to manage, and also more expensive. Thus, this kind of rosette is not commonly used despite its inherent advantage. Nau and Scholtes[39] reported a rosette with up to eight grids and discussed how to connect them in different configurations and also highlighted the reduced sensitivity on the hole eccentricity. The rosette type C reported in the ASTM standard also has an opposite grid for each of the three directions; however, one side is radial and the other side is along the hoop direction. For this reason, the interaction is opposed to the compensation since the strain measured on one side has the opposite sign with respect to the other side; indeed, each couple of strain-gages has to be connected as half-bridge. On the contrary, the ring core method is another interesting example of compensating eccentricity. The three grids are attached to the inside volume; thus, the eccentricity produces a smaller distance from the annular cut in one region and a higher distance in the opposite region of the grid. Therefore, the sensitivity of each grid is compensated for and the first-order matrices $\bar{\alpha}_{e1}, \bar{\alpha}_{e3}$ are 0. This means that the procedure p, q, t with decoupled components can be followed regardless of even relatively large eccentricities.

For common hole-drilling, without any compensating extra grid, the problem reformulated according to equation (9) seems to require many terms. In reality, the symmetry properties reduce the number of *free* parameters of the matrix $\bar{\mathbf{A}}$ and its derivatives, thus making the approach more accessible. Matrix $\bar{\mathbf{A}}_0$, which is matrix $\bar{\mathbf{A}}$ in the case of no eccentricity, is a combination of the coefficients of the two matrices $\bar{\mathbf{a}}$ and $\bar{\mathbf{b}}$ previously introduced. It is thus an 'inflated' reissue (since it has more coefficients) of $\bar{\mathbf{a}}$ and $\bar{\mathbf{b}}$. but offers a framework for the extension to the eccentricity problem. The following relationship (which is equivalent to equation (2)) offers the easiest way to calculate the coefficients of this matrix

$$\begin{bmatrix} A^{(ij)}_{0,11} & A^{(ij)}_{0,12} & A^{(ij)}_{0,13} \\ A^{(ij)}_{0,21} & A^{(ij)}_{0,22} & A^{(ij)}_{0,23} \\ A^{(ij)}_{0,31} & A^{(ij)}_{0,32} & A^{(ij)}_{0,33} \end{bmatrix} = \begin{bmatrix} \frac{(1+\nu)a_{ij}+b_{ij}}{2} & \frac{(1+\nu)a_{ij}-b_{ij}}{2} & 0 \\ \frac{(1+\nu)a_{ij}}{2} & \frac{(1+\nu)a_{ij}}{2} & b_{ij} \\ \frac{(1+\nu)a_{ij}-b_{ij}}{2} & \frac{(1+\nu)a_{ij}+b_{ij}}{2} & 0 \end{bmatrix} \tag{17}$$

Equation (17) only shows a single block of the matrix $\bar{\mathbf{A}}_0$; anyway, this reconstruction is valid for all the blocks on the diagonal $i = j$ and for any other block below the diagonal $i > j$. A symmetry property also relates matrices $\bar{\alpha}_{e1}$ and $\bar{\alpha}_{e3}$. Given the angular pattern $0°, 225°(45°), 90°$ of the grids, the derivation terms with respect to the components of eccentricity are the same but in different positions. Thus, one of the two can be obtained by the other just through simple permutations of the coefficients. For example, if $\bar{\alpha}_{e1}$ is already available, $\bar{\alpha}_{e3}$ is obtained by the following matrix equation (this relationship is only valid for a CCW system of directions 1 and 3)

$$\bar{\alpha}_{e3} = \bar{\mathbf{P}}_L \bar{\alpha}_{e1} \bar{\mathbf{P}}_R \tag{18}$$

in which $\bar{\mathbf{P}}_L$ and $\bar{\mathbf{P}}_R$ are the two permutation *left* and *right* matrices, respectively, and they are 3×3 block diagonal containing only 0 and 1 in specific positions. The following is an example with three blocks of these permutation matrices

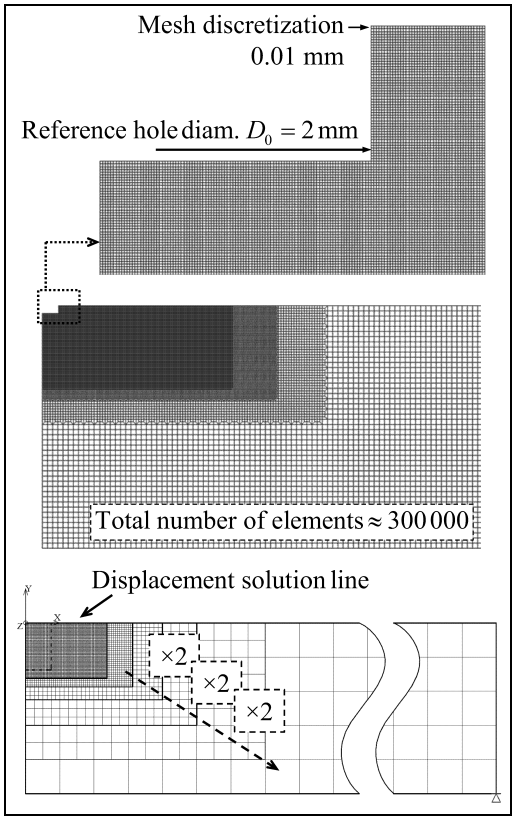

Figure 3. Plane FE model with axial-symmetric harmonic elements and multiple nested refinements.

$$\bar{\mathbf{P}}_{\mathrm{L}} = \left[\begin{array}{ccc|ccc|ccc} 0 & 0 & 1 & 0 & 0 & 0 & 0 & 0 & 0 \\ 0 & 1 & 0 & 0 & 0 & 0 & 0 & 0 & 0 \\ 1 & 0 & 0 & 0 & 0 & 0 & 0 & 0 & 0 \\ \hline 0 & 0 & 0 & 0 & 0 & 1 & 0 & 0 & 0 \\ 0 & 0 & 0 & 0 & 1 & 0 & 0 & 0 & 0 \\ 0 & 0 & 0 & 1 & 0 & 0 & 0 & 0 & 0 \\ \hline 0 & 0 & 0 & 0 & 0 & 0 & 0 & 0 & 1 \\ 0 & 0 & 0 & 0 & 0 & 0 & 0 & 1 & 0 \\ 0 & 0 & 0 & 0 & 0 & 0 & 1 & 0 & 0 \end{array}\right], \quad \bar{\mathbf{P}}_{\mathrm{R}} = \left[\begin{array}{ccc|ccc|ccc} 0 & 1 & 0 & 0 & 0 & 0 & 0 & 0 & 0 \\ 1 & 0 & 0 & 0 & 0 & 0 & 0 & 0 & 0 \\ 0 & 0 & 1 & 0 & 0 & 0 & 0 & 0 & 0 \\ \hline 0 & 0 & 0 & 0 & 1 & 0 & 0 & 0 & 0 \\ 0 & 0 & 0 & 1 & 0 & 0 & 0 & 0 & 0 \\ 0 & 0 & 0 & 0 & 0 & 1 & 0 & 0 & 0 \\ \hline 0 & 0 & 0 & 0 & 0 & 0 & 0 & 1 & 0 \\ 0 & 0 & 0 & 0 & 0 & 0 & 1 & 0 & 0 \\ 0 & 0 & 0 & 0 & 0 & 0 & 0 & 0 & 1 \end{array}\right] \tag{19}$$

Finite element modelling

A parametric finite element (FE) model was implemented to determine the coefficients of the matrices introduced above. The axial-symmetric geometry enabled structural plane harmonic elements (ANSYS Plane25) to be used. A full three-dimensional model, as proposed by Aoh and Wei[44] and Xiao and Rong,[45] was avoided in order to produce a very high spatial resolution in the region of interest with multiple nested refinements (Figure 3). The mesh division at the hole region was as small as one-hundredth of the radius, which was assumed equal to 1 mm as reference. The accuracy of the FE model was estimated to be approximately 1%, by comparing the numerical results with the analytical solution of the Kirsch equations, after reducing (just for benchmarking) the model height to a single row of elements and simulating a plane stress problem.

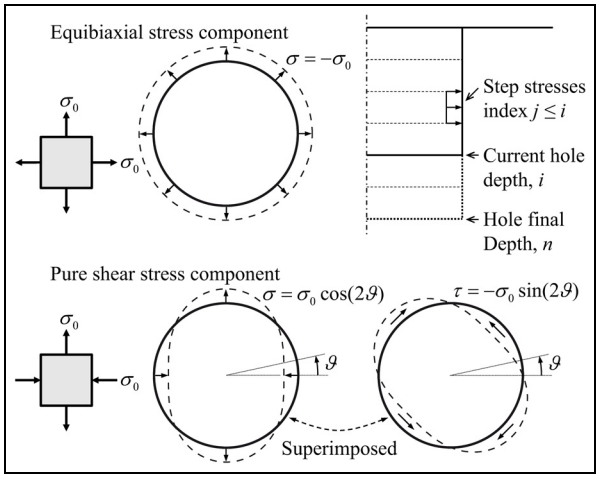

Figure 4. Simulation of material removal for the equibiaxial and the pure shear stress load types.

Two types of load were imposed on the axial-symmetric harmonic model: equibiaxial and pure shear. As reported in Figure 4, the equibiaxial was obtained with the harmonic order zero, while the pure shear was obtained with the harmonic order 2, which is the tensorial dependence. To obtain the first load type, the removal of material with residual stress embedded was simulated as the application of pressure on the free cylindrical surface of the hole. Then, the pure shear was obtained as pressure (symmetric with respect to $\vartheta = 0$ angular coordinate) superimposed on a distribution of tangential traction with a relative phase equal to 45° (anti-symmetric). These two load conditions, applied as uniform steps at different hole increments, enabled all the calibration coefficients to be obtained. Initially, without eccentricity, the procedure for a_{ij} and b_{ij} coefficients required the evaluation of p and q strain components, respectively, given by the combination of directions 1 and 3 alone. On the other hand, all the grids were considered for the more general case with eccentricity, and the stresses σ_x and σ_y were obtained as the subtraction and sum of the equibiaxial and shear components, respectively.

According to equations (7) and (9), the calibration coefficients can be interpreted as the relaxed strains induced by unitary residual stresses. The strains measured by the grids were numerically simulated from the FE analysis displacements by considering the angular ϑ dependence. The displacement fields on the upper

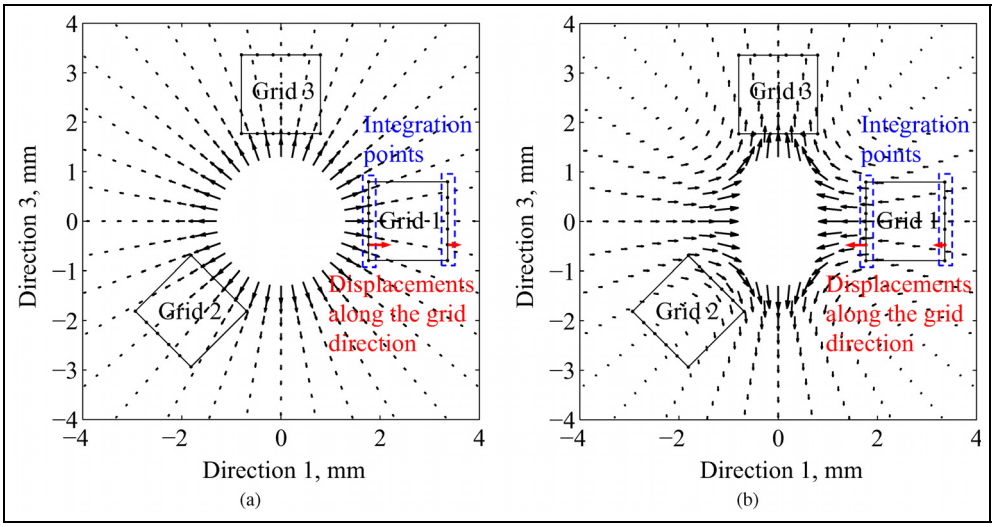

Figure 5. Type A rosette, displacement fields for (a) the equibiaxial and (b) the pure shear load components.

surface are shown in Figure 5 for the two load types. The displacements along the grid direction, which is slightly different from the radial direction due to the grid width, were calculated and averaged at several integration points along the two opposite sides of the grid. The strain was obtained by computing the difference of the averages at the two sides and finally by dividing by the grid length. This calculation is easier and faster and still equal to computing the average strain over the whole grid area, and for more details see, in particular, Nau and Scholtes.[39] Finally, this numerical analysis was also performed with eccentricity, following the same procedure, after updating the actual position of the grids with respect to the hole centre. A square array of eccentricity component values has been considered in order to obtain the (numerical) derivatives of the calibration coefficients.

Calibration coefficient matrices

Standard calibration coefficients with no eccentricity

Although already available on the ASTM E837 standard,[31] the calibration matrices $\bar{\mathbf{a}}$ and $\bar{\mathbf{b}}$ were recalculated as a benchmark of the numerical procedure, and also to provide an update of the coefficients with the very accurate FE model shown above. The exact combination of rosette dimensions, hole diameter and hole depth step is required to validate any single set of a_{ij} and b_{ij} calibration coefficients. The choice of other dimension ratios involves different coefficients, which need the calculation to be repeated. In fact, the use of an automated algorithm is recommended whereby any geometry configuration can be inputted to generate these coefficients.[41,42] The specific dimensional combinations reported in the ASTM standard are considered here, and the calibration coefficients are provided in Tables 1–4 of the online Appendix (available at: http://sdj.sagepub.com/), for type A and type B rosettes. The ASTM standard suggests the use of either millimetres or inches as length units, however, with a simplified rounding. The coefficients according to both the standard millimetres and inch dimensions were calculated and can be found in the tables in the online Appendix. The effect of the approximated conversion was quantified and the coefficient differences are in the order of a few percentage points up to 5%. Using inches, a comparative analysis between the calculated coefficients with this model and the values reported in the ASTM standard is provided in Figure 6 for type A. The histograms highlight that the differences are limited to a few percentage points mainly at, and near to, the matrix diagonal. Very similar comparison results were also obtained for type B.

The role of the Poisson's ratio ν as reported in equation (7) is valid, in principle, only for the plane stress problem, which is a very accurate approximation of the through-thickness hole on a thin plate. As discussed above, the calibration coefficients actually have a more general dependence with respect to the Poisson's ratio and the plane stress form is only approximated. In order to quantify the error introduced by assuming no dependence of the coefficients on the Poisson's ratio, the FE analysis was repeated with $\nu = 0.35$ and the coefficients were recalculated accordingly. This comparison analysis returned similar coefficient values, and again two histograms with percentage differences are reported in Figure 7. These differences are still in the order of a few percentage points, and the highest discrepancies are for the initial depths. Similar results were also obtained by Nau et al.[46] confirming the validity of this analysis. The usual structural metal alloys never show very large Poisson's ratio differences from the reference $\nu = 0.3$ value. Thus, the form of equation (7) can be considered as satisfactorily accurate, after substituting the appropriate value of ν for the specific material, and using the calibration coefficients derived with $\nu = 0.3$. In fact, all the coefficients in the tables in the online Appendix are reported for reference $\nu = 0.3$ alone.

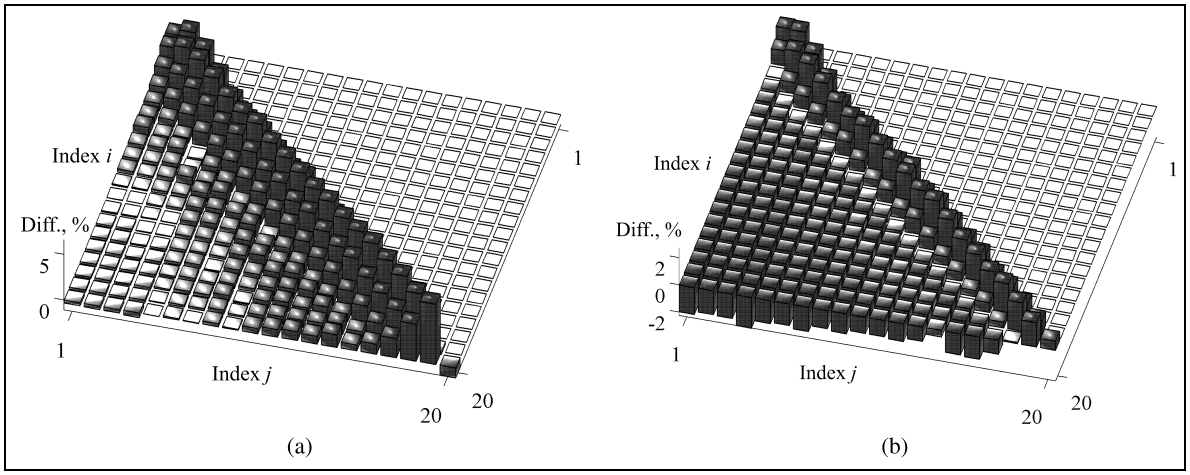

Figure 6. Percentage differences obtained with respect to the ASTM type A, a_{ij} and b_{ij} in (a) and (b), respectively.

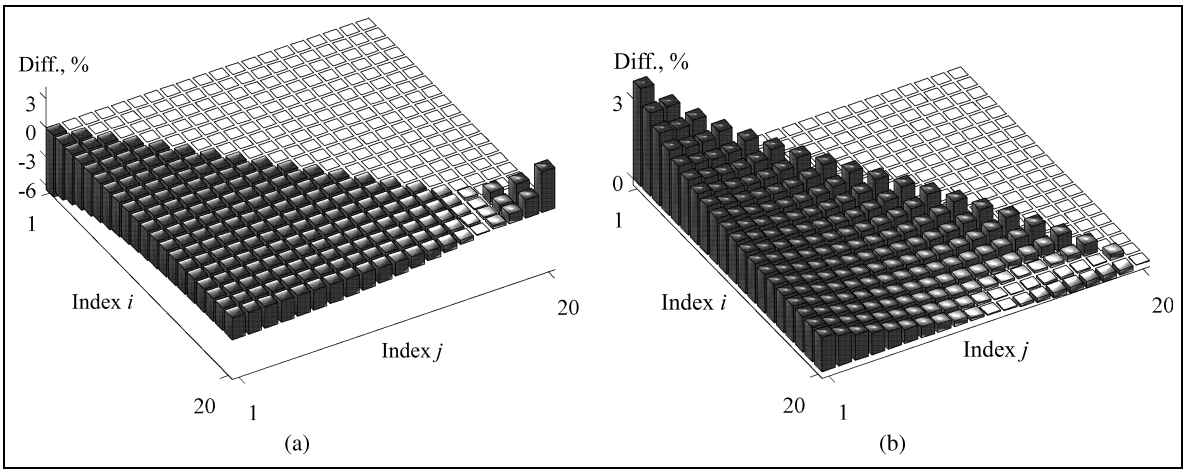

Figure 7. Percentage differences for the Poisson's ratio, a_{ij} and b_{ij} in (a) and (b), respectively, comparing $\nu = 0.35$ coefficients with the reference $\nu = 0.3$.

First-order correction for eccentricity

All the coefficients in matrix $\bar{\mathbf{A}}$ were calculated for an array of eccentricities using directions 1 and 3 as reference system. Initially, a large eccentricity range ± 0.3 mm was considered for the rosette diameter $D = 5.13$ mm. As an example, Figure 8(a) shows the dependence of a single coefficient of the matrix, and similar trends were obtained for all the other coefficients. The dependency of the coefficients on the eccentricity is essentially linear thus, according to equation (11), the higher order terms introduce a further contribution which turns out to be minor, especially near the zero eccentricity origin. By reducing the investigated eccentricity range to ± 0.05 mm, which is still more than twice the eccentricity allowed by the ASTM standard, Figure 8(b) highlights that the linear dependency is an extremely accurate model and the residual difference is negligible. On the other hand, if a second compensating grid is introduced for each direction, or another self-compensating problem is investigated such as the ring core method, the tangent plane at the origin is perfectly horizontal as the first-order partial derivatives are 0. In these cases, the higher order terms still play a marginal role, thus the p, q, t procedure is accurate and the proposed generalization is unnecessary. The matrix $\bar{\alpha}_{e1}$ was calculated by (numerically) determining the partial derivatives on the small range of Figure 8(b) and just by considering a single eccentricity component, specifically direction 1. The coefficients of the matrix $\bar{\alpha}_{e1}$ are listed in Tables 5 and 6 of the online Appendix (available at: http://sdj.sagepub.com/), for the ASTM standard type A and type B rosettes, respectively. The other derivative matrix $\bar{\alpha}_{e3}$ can be easily calculated from equation (18), and finally the matrix $\bar{\mathbf{A}}$ is obtained with equation (15). When a generic couple of eccentricity components is introduced, the matrix $\bar{\mathbf{A}}$ has no more 0 values at or below the block diagonal; hence, the proposed method is effectively exploited.

The Poisson's ratio dependence of matrix $\bar{\mathbf{A}}_0$ is given by equation (17). The appropriate value of ν can be introduced in the calculation of each block along with the coefficients of the matrices $\bar{\mathbf{a}}$ and $\bar{\mathbf{b}}$. However, the

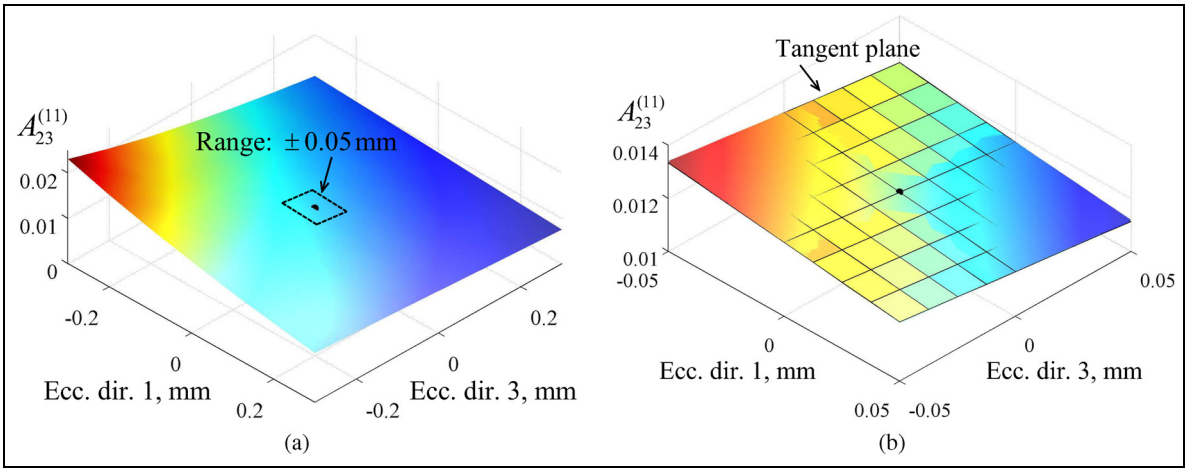

Figure 8. Eccentricity dependence of a single coefficient of matrix $\bar{A}$: (a) trend on a large range and (b) tangent plane on a small range.

derivative matrix coefficient dependence on the Poisson's ratio is more complicated since the equibiaxial and the shear stress components are coupled. Thus, there is no simple equation to take into account the Poisson's ratio for the derivative matrices, and the coefficients reported in Tables 5 and 6 of the online Appendix (available at: http://sdj.sagepub.com/), are just defined for $\nu = 0.3$. A recalculation would be needed for any different values of ν. However, the Poisson's ratio is usually very close to $\nu = 0.3$, at least for metals, as already discussed above. In addition, the derivative matrices only provide a correction for matrix $\bar{\mathbf{A}}$; thus, the effect on the final result of a small variation in the Poisson's ratio is marginal.

Validation analysis

Numerical tests are proposed in this section to validate the introduced eccentricity correction procedure. Using the algorithm developed by Beghini et al.[41,42] based on influence functions, any residual stress distribution can be simulated solving the *direct* problem and the relaxed strains along the depth predicted. The residual stress distribution, which is assumed as being uniform for the sake of simplicity, was initially back-calculated with the integral method according to the standard, applying the usual p, q, t procedure and neglecting the eccentricity. The calculation was then repeated by introducing the linear correction for matrix $\bar{\mathbf{A}}$ and solving the inverse problem (equation (16)). Initially, a calculation example was performed with both the eccentricity components being not 0 and not equal. The eccentricities introduced were in the order of a few hundredths of millimetres, similar to the values in real tests with $D = 5.13$ mm rosettes.[32,47] The first calculation was implemented with the type A rosette and eccentricity components $e_1 = -0.02$ mm and $e_3 = 0.05$ mm; thus, the overall eccentricity is larger than the limit prescribed by the standard: $\sqrt{e_1^2 + e_3^2} > 0.02$ mm. The eccentricity introduced a perceptible error with respect to the reference stresses (Figure 9(a)); then this error was almost completely eliminated after introducing the linear correction (Figure 9(b)), therefore confirming the effectiveness of the proposed procedure and the accuracy of the coefficients provided. The second calculation was repeated with the same reference residual stresses but with type B rosette and just a single component of eccentricity, which, however, was 10 times larger than the limit allowed by the standard. Maximum stress error in the order of 40% was obtained as the result of the p, q, t procedure, thus meaning a considerable effect due to the large eccentricity (Figure 10(a)). As highlighted in Figure 8, the linear component represents the actual trend of the coefficients very well even for relatively large eccentricities. Thus, the stress reconstruction with the linear correction was still quite accurate, returning a marginal residual error similar to the first example without any correction (Figure 10(b)).

A wider analysis was then performed to test the effect of eccentricity and verify the correction introduced by the procedure, covering all the combinations of eccentricity values and stresses. Six levels of eccentricity were considered: $e_1, e_3 = 0.02, 0.05, 0.07, 0.10, 0.15, 0.20$ mm and with 16 angular positions for each: $0.0°, 22.5°, \ldots, 337.5°$. For all the combinations of eccentricity radius and angle, three tests were separately simulated for the stresses $\sigma_x, \sigma_y, \tau_{xy} = 100$ MPa. The highest percentage difference was found along the depth coordinate and saved for all the eccentricity and stress combinations for both type A and type B rosettes. This calculation was then repeated for the same combinations of eccentricity and stresses applying the correction procedure. Figure 11 highlights that the maximum eccentricity errors increased linearly with the eccentricity, while the correction reduced the residual error by limiting it to a few percentage points even for an eccentricity as large as $0.1 - 0.15$ mm, which is quite high with respect to the usual best practice in the experiments. The larger grid width of type A rosette averages the strain distribution better; thus, type B rosette experiences a higher eccentricity sensitivity when the

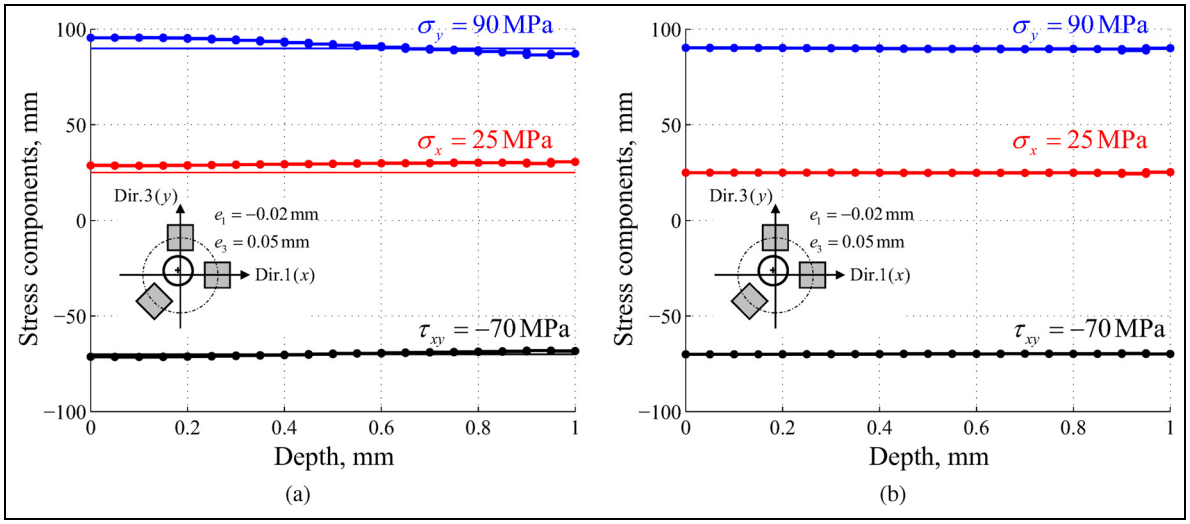

Figure 9. Validation example with type A rosette: (a) error caused by the eccentricity and (b) almost perfect result with the first-order correction.

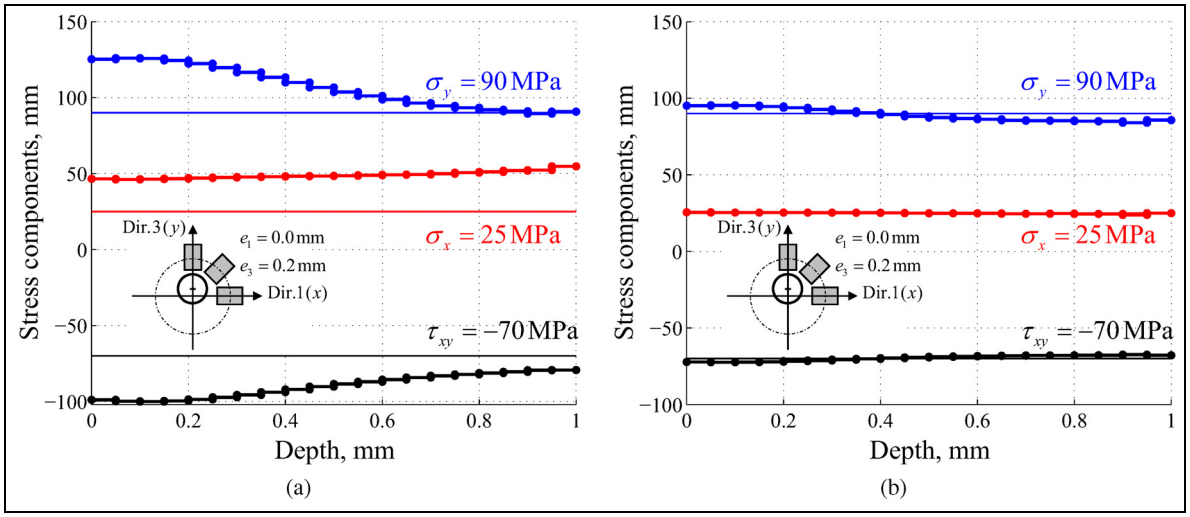

Figure 10. Validation example with type B rosette: (a) error caused by a large eccentricity and (b) accurate result with the first-order correction.

standard integral method is applied. With the proposed correction, the higher sensitivity of type B rosette is only evident for large eccentricity values, while in the range where the linearity is predominant, the small residual error is very similar for the two rosette types.

Conclusion

We have described a generalization of the hole-drilling integral method, which includes a correction for the eccentricity of the hole with respect to the strain-gage rosette. The eccentricity impairs the axial symmetry of the problem; thus, the decoupling of the stress components in an equibiaxial plus two shear stresses is no longer allowed. Consequently, a single matrix is needed to linearly relate the relaxed strains to the residual stress components. After having grouped the strains and the stresses in vectors along the depth, this matrix is a lower triangular 3×3 block, and each of its coefficients can be expressed as a power series of the eccentricity components. The two linear terms alone already proved to be a very accurate model for reproducing the eccentricity effect. The matrix was then expressed as the zero eccentricity term plus a linear correction of the two eccentricity components by introducing the derivative matrices. In addition, the $0°, 225°(45°), 90°$ grid pattern only requires the knowledge of a single derivative matrix, while the other can be obtained as a permutation of the coefficients, for symmetry reasons. On the other hand, if a compensating grid is applied for each direction, the first-order derivatives are 0 (similarly to the ring core method) and the problem can still be formulated with the usual combined stresses and strains.

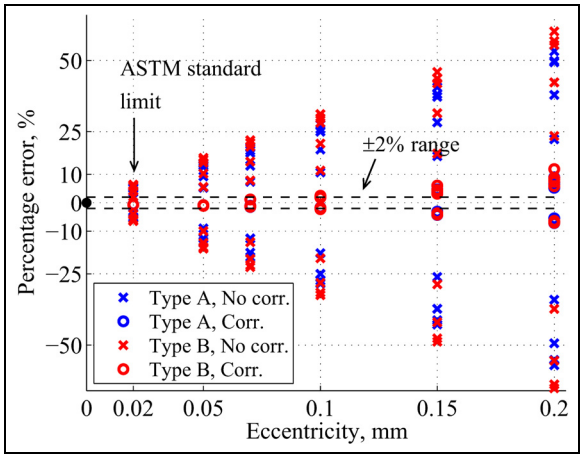

Figure 11. Maximum percentage errors for several combinations of eccentricity positions and stresses, and corrections obtained with the proposed procedure.

A very refined plane and axial-symmetric harmonic FE model was implemented and the calibration coefficients were calculated. Initially, a revision of the ASTM standard was proposed, according to the combined stresses and strains. The derivative matrices were then calculated and provided for both type A and type B strain-gage rosettes. Finally, an extensive numerical analysis was proposed both to validate the procedure and to show the accuracy of the correction. When the eccentricity is in the order of the small allowed limit prescribed by the standard, the reconstruction of the stress components with the eccentricity correction is very accurate. However, if the eccentricity is small, its measure uncertainty can be of the same entity of the eccentricity itself; thus, the present correction is not recommended. On the other hand, quite accurate results were still obtained with larger eccentricities, approximately up to 10 times the standard limit, since the linear first order is a fine model even for relatively high eccentricity values. In conclusion, the proposed procedure can significantly increase the eccentricity allowed and, even when the hole is produced with a large offset for any experimental reason, the measure can still be useful instead of being discarded or repeated.

Declaration of conflicting interests

The author(s) declared no potential conflicts of interest with respect to the research, authorship and/or publication of this article.

Funding

The author(s) disclosed receipt of the following financial support for the research, authorship, and/or publication of this article: This work was supported by the University of Pisa under the 'PRA – Progetti di Ricerca di Ateneo' (Institutional Research Grants) – Project No. PRA_2016_36.

References

1. Withers PJ. Residual stress and its role in failure. *Rep Prog Phys* 2007; 70: 2211–2264.
2. Withers PJ and Bhadeshia HKDH. Residual stress part 1 – measurement techniques. *Mater Sci Tech* 2001; 17: 355–365.
3. Prime MB. The contour method: a new approach in experimental mechanics. In: *Society for experimental mechanics – SEM annual conference and exposition on experimental and applied mechanics 2009*, Albuquerque, NM, 1–4 June 2009, vol. 3, pp.1621–1629, http://sem-proceedings.com/09s/sem.org-SEM-2009-Ann-Conf-s074p01-Keynote-Presentation-40-minutes-The-Contour-Method-A-New-Approach.pdf
4. Barsanti M, Beghini M, Santus C, et al. Integral method coefficients and regularization procedure for the ring-core residual stress measurement technique. *Adv Mat Res* 2014; 996: 331–336.
5. Menda F, Trebuňa F and Šarga P. Determination of the necessary geometric parameters of the specimen in Ring-Core method. *Appl Mech Mater* 2014; 486: 90–95.
6. Šarga P, Menda F and Trebuňa F.. Experimental verification of the geometric parameters in the ring-core measurement. In: *EAN 2015 – 53rd conference on experimental stress analysis*, Český Krumlov, 1–4 June 2015, pp.388–394. Praha: Czech Society for Mechanics.
7. Stefanescu D, Truman CE and Smith DJ. An integrated approach for measuring near-surface and subsurface residual stress in engineering components. *J Strain Anal Eng* 2004; 39: 483–497.
8. Dattoma V, De Giorgi M and Nobile R. On the evolution of welding residual stress after milling and cutting machining. *Comput Struct* 2006; 84: 1965–1976.
9. Venkitakrishnan PV, Philip J and Krishnamurthy R. An assessment of stresses in thin walled welded tubes through hole drilling and sectioning methods. *J Mater Process Tech* 2007; 185: 228–232.
10. Hosseinzadeh F, Mahmoudi AH, Truman CE, et al. Application of deep hole drilling to the measurement and analysis of residual stresses in steel shrink-fitted assemblies. *Strain* 2011; 47: 412–426.
11. Zuccarello B and Di Franco G. Numerical-experimental method for the analysis of residual stresses in cold-expanded holes. *Exp Mech* 2013; 53: 673–686.
12. Buljak V, Cocchetti G, Cornaggia A, et al. Assessment of residual stresses and mechanical characterization of materials by 'hole drilling' and indentation tests combined and by inverse analysis. *Mech Res Commun* 2015; 68: 18–24.
13. Schajer GS and Prime MB. Use of inverse solutions for residual stress measurements. *J Eng Mater: T ASME* 2006; 128: 375–382.
14. Prime MB and Hill MR. Uncertainty, model error, and order selection for series-expanded, residual-stress inverse solutions. *J Eng Mater: T ASME* 2006; 128: 175–185.
15. Schajer GS. Advances in hole-drilling residual stress measurements. *Exp Mech* 2010; 50: 159–168.
16. Schajer GS. Hole-drilling residual stress measurements at 75: origins, advances, opportunities. *Exp Mech* 2010; 50: 245–253.
17. Schajer GS and Steinzig M. Full-field calculation of hole drilling residual stresses from electronic speckle pattern interferometry data. *Exp Mech* 2005; 45: 526–532.

18. Baldi A. Full field methods and residual stress analysis in orthotropic material. I Linear approach. *Int J Solids Struct* 2007; 44: 8229–8243.
19. Jahed H, Faritus MR and Jahed Z. Residual stress measurements in an autofrettage tube using hole drilling method. *J Press Vess: T ASME* 2012; 134: 051501.
20. Nobre JP, Dias AM, Gibmeier J, et al. Local stress-ratio criterion for incremental hole-drilling measurements of shot-peening stresses. *J Eng Mater: T ASME* 2006; 128: 193–201.
21. Beghini M, Bertini L, Monelli BD, et al. Experimental parameter sensitivity analysis of residual stresses induced by deep rolling on 7075-T6 aluminium alloy. *Surf Coat Technol* 2014; 254: 175–186.
22. Valente T, Bartuli C, Sebastiani M, et al. Implementation and development of the incremental hole drilling method for the measurement of residual stress in thermal spray coatings. *J Therm Spray Techn* 2005; 14: 462–470.
23. Dorman M, Toparli MB, Smyth N, et al. Effect of laser shock peening on residual stress and fatigue life of clad 2024 aluminium sheet containing scribe defects. *Mat Sci Eng A* 2012; 548: 142–151.
24. Obelode E and Gibmeier J. Residual stress analysis on thick film systems by the incremental hole-drilling method – Simulation and experimental results. *Exp Mech* 2013; 53: 965–976.
25. Held E and Gibmeier J. Residual stress analysis of thick film systems by the incremental hole-drilling method. *HTM: J Heat Treat Mater* 2014; 69: 71–79.
26. Schajer GS. Measurement of non-uniform residual stresses using the hole-drilling method. Part I: stress calculation procedures. *J Eng Mater: T ASME* 1988; 110: 338–343.
27. Schajer GS. Measurement of non-uniform residual stresses using the hole-drilling method. Part II: practical application of the integral method. *J Eng Mater: T ASME* 1988; 110: 344–349.
28. Andersen LF. Experimental method for residual stress evaluation through the thickness of a plate. *J Eng Mater: T ASME* 2002; 124: 428–433.
29. Held E, Schuster S and Gibmeier J. Incremental hole-drilling method vs. thin components: a simple correction approach. *Adv Mat Res* 2014; 996: 283–288.
30. Schajer GS and Rickert TJ. Incremental computation technique for residual stress calculations using the integral method. *Exp Mech* 2011; 51: 1217–1222.
31. ASTM E837-13a:2013. Standard test method for determining residual stresses by the hole-drilling strain-gage method.
32. Valentini E, Beghini M, Bertini L, et al. Procedure to perform a validated incremental hole drilling measurement: application to shot peening residual stresses. *Strain* 2011; 47: e605–e618.
33. Valentini E, Benincasa A and Santus C. Bending test rig for validating the hole drilling method residual stress measurement. *Mater Sci Forum* 2014; 768–769: 150–157.
34. Casavola C, Pappalettera G, Pappalettere C, et al. Analysis of the effects of strain measurement errors on residual stresses measured by incremental hole-drilling method. *J Strain Anal Eng* 2013; 48: 313–320.
35. Schajer GS. Hole-drilling residual stress profiling with automated smoothing. *J Eng Mater: T ASME* 2007; 129: 440–445.
36. Beghini M, Bertini L and Santus C. A procedure for evaluating high residual stresses using the blind hole drilling method, including the effect of plasticity. *J Strain Anal Eng* 2010; 45: 301–318.
37. Beghini M, Santus C, Valentini E, et al. Experimental verification of the hole drilling plasticity effect correction. *Mater Sci Forum* 2011; 681: 151–158.
38. Scafidi M, Valentini E and Zuccarello B. Error and uncertainty analysis of the residual stresses computed by using the hole drilling method. *Strain* 2011; 47: 301–312.
39. Nau A and Scholtes B. Evaluation of the high-speed drilling technique for the incremental hole-drilling method. *Exp Mech* 2013; 53: 531–542.
40. Ajovalasit A. Measurement of residual stresses by the hole-drilling method: influence of hole eccentricity. *J Strain Anal Eng* 1979; 14: 171–178.
41. Beghini M, Bertini L, Mori LF, et al. Definition and validation of the influence functions. *Strain* 2010; 46: 324–336.
42. Beghini M, Bertini L and Mori LF. Evaluating non-uniform residual stress by the hole-drilling method with concentric and eccentric holes. Part II: application of the influence functions to the inverse problem. *Strain* 2010; 46: 337–346.
43. Beghini M, Bertini L, Santus C, et al. Validazione sperimentale di una rosetta a 6 griglie per ridurre l'errore di eccentricità nella misura delle tensioni residue. In: *Congresso AIAS XXXIX*, 2010.
44. Aoh J-N and Wei C-S. On the improvement of calibration coefficients for hole-drilling integral method. Part I: Analysis of calibration coefficients obtained by a 3-D FEM model. *J Eng Mater: T ASME* 2002; 124: 250–258.
45. Xiao B, Li K and Rong Y. Numerical study on calibration coefficients for hole-drilling residual stress measurement. In: *Society for experimental mechanics – SEM annual conference and exposition on experimental and applied mechanics 2009*, Albuquerque, NM, 1–4 June 2009, vol. 2, pp.990–997, http://sem-proceedings.com/09s/sem.org-SEM-2009-Ann-Conf-s044p03-Numerical-Study-Calibration-Coefficients-Hole-drilling-Residual.pdf
46. Nau A, von Mirbach D and Scholtes B. Improved calibration coefficients for the hole-drilling method considering the influence of the Poisson ratio. *Exp Mech* 2013; 53: 1371–1381.
47. Ajovalasit A, Scafidi M, Zuccarello B, et al. The hole-drilling strain gauge method for the measurement of uniform or non-uniform residual stresses. In: *Conference AIAS XXXIX*, Technical Report TR01, 2010. AIAS.

Appendix 1

Notation

$\bar{\mathbf{A}}$	calibration coefficient 3×3 block matrix
a, b	calibration coefficients relating the P, Q, T residual stresses to the p, q, t relaxed strains
$\bar{\mathbf{a}}, \bar{\mathbf{b}}$	calibration coefficient matrices relating the combined residual stresses and the relaxed strains
A, B	general elastic constants relating the residual stresses to the relaxed strains
D	average diameter of the strain-gage rosette
$\mathbf{e}$	vectors containing the blocks of the three grid relaxed strains

E, ν	Young's modulus and Poisson's ratio of the isotropic linear elastic material
h, k	block indexes, for the matrix $\bar{\mathbf{A}}$, ranging from 1 to 3
i, j	calibration matrix depth indexes, $i = 1, \ldots, n$ and $j = 1, \ldots, i$
n	number of hole increments at the final depth
p, q, t	combined relaxed strains according to the P, Q, T stresses
$\mathbf{p}, \mathbf{q}, \mathbf{t}$	vectors containing the combined strains along the depth arranged in blocks
P, Q, T	equibiaxial and shear combined stresses
$\mathbf{P}, \mathbf{Q}, \mathbf{T}$	vectors containing the combined stresses along the depth arranged in blocks
$\mathbf{S}$	vectors containing the blocks of the three uncombined residual stress components

Greek symbols

$\bar{\alpha}_{e1}, \bar{\alpha}_{e3}$	derivative matrices for the calibration coefficient correction of 1 and 3 directions, respectively
ΔZ	hole depth incremental step
ε_r	relaxed strain measured by a generic grid
$\varepsilon_1, \varepsilon_2, \varepsilon_3$	relaxed strains measured by the 0°, 225°(45°), 90° grids
η_1, η_3	dimensionless eccentricity components
$\sigma_{max}, \sigma_{min}$	principal maximum and minimum residual stresses
$\sigma_x, \sigma_y, \tau_{xy}$	residual stress components according to the rosette reference frame
ϑ	generic grid orientation with respect to the maximum principal stress direction

Subscripts

$\bar{\mathbf{A}}_0$	calibration coefficient matrix $\bar{\mathbf{A}}$ with zero eccentricity
D_0	drilled hole diameter
e_1, e_3	eccentricity components along the directions 1 (x) and 3 (y)
G_L, G_W	strain-gage rosette grid length and grid width
$\bar{\mathbf{P}}_L, \bar{\mathbf{P}}_R$	left and right 3×3 block permutation matrices

Online Appendix:

Michele Barsanti, Marco Beghini, Leonardo Bertini, Bernardo D Monelli, and Ciro Santus

First-order correction to counter the effect of eccentricity on the hole-drilling integral method with strain-gage rosettes

The Journal of Strain Analysis for Engineering Design 0309324716649529, first published on June 8, 2016
doi:10.1177/0309324716649529

Table 1. Type A rosette, ASTM E837–13a, $D = 5.13$ mm, $G_L = 1.59$ mm, $G_W = 1.59$ mm, $D_0 = 2.0$ mm, $\Delta Z = 0.05$ mm.

Matrix $\bar{\mathbf{a}}$ coefficients ($\times 10^3$)

6.613																			
7.932	7.099																		
9.040	8.359	7.296																	
10.018	9.360	8.540	7.291																
10.886	10.230	9.473	8.521	7.132															
11.654	10.994	10.263	9.400	8.342	6.856														
12.331	11.666	10.945	10.125	9.172	8.036	6.491													
12.926	12.256	11.538	10.740	9.840	8.818	7.633	6.065												
13.447	12.771	12.054	11.267	10.397	9.434	8.367	7.159	5.598											
13.900	13.219	12.502	11.721	10.868	9.940	8.935	7.846	6.640	5.110										
14.294	13.609	12.889	12.113	11.270	10.363	9.395	8.369	7.279	6.093	4.614									
14.635	13.946	13.224	12.449	11.613	10.719	9.774	8.786	7.758	6.686	5.538	4.124								
14.929	14.237	13.513	12.738	11.907	11.021	10.091	9.127	8.137	7.125	6.085	4.986	3.649							
15.183	14.488	13.762	12.987	12.157	11.278	10.358	9.410	8.443	7.467	6.485	5.489	4.449	3.194						
15.402	14.704	13.976	13.200	12.372	11.496	10.583	9.645	8.695	7.742	6.795	5.853	4.909	3.933	2.766					
15.590	14.890	14.160	13.383	12.555	11.681	10.773	9.843	8.903	7.967	7.041	6.132	5.239	4.353	3.445	2.366				
15.752	15.049	14.318	13.539	12.711	11.839	10.934	10.008	9.077	8.151	7.241	6.352	5.490	4.651	3.826	2.988	1.996			
15.891	15.186	14.453	13.673	12.845	11.973	11.070	10.148	9.222	8.304	7.404	6.530	5.687	4.876	4.095	3.333	2.563	1.656		
16.010	15.304	14.569	13.788	12.959	12.088	11.186	10.266	9.344	8.431	7.538	6.674	5.845	5.052	4.297	3.574	2.874	2.172	1.347	
16.112	15.405	14.668	13.886	13.056	12.185	11.284	10.366	9.446	8.537	7.649	6.792	5.972	5.192	4.453	3.754	3.091	2.452	1.814	1.067

Matrix $\bar{\mathbf{b}}$ coefficients ($\times 10^3$)

12.231																			
14.104	13.199																		
15.700	15.074	13.749																	
17.137	16.593	15.665	14.003																
18.438	17.938	17.139	15.949	14.021															
19.612	19.143	18.412	17.382	15.977	13.850														
20.665	20.222	19.535	18.591	17.366	15.792	13.525													
21.605	21.184	20.528	19.639	18.512	17.130	15.433	13.081												
22.439	22.038	21.407	20.556	19.490	18.213	16.714	14.937	12.546											
23.175	22.793	22.181	21.357	20.335	19.124	17.734	16.156	14.336	11.948										
23.822	23.456	22.860	22.059	21.067	19.902	18.580	17.111	15.489	13.660	11.308									
24.387	24.036	23.455	22.671	21.702	20.570	19.295	17.895	16.381	14.745	12.935	10.645								
24.880	24.542	23.974	23.203	22.253	21.145	19.904	18.551	17.105	15.575	13.951	12.182	9.975							
25.308	24.982	24.425	23.666	22.730	21.641	20.424	19.106	17.706	16.242	14.720	13.129	11.419	9.310						
25.678	25.364	24.815	24.067	23.143	22.068	20.871	19.577	18.210	16.791	15.333	13.839	12.298	10.659	8.658					
25.998	25.693	25.154	24.413	23.499	22.436	21.253	19.978	18.637	17.250	15.835	14.402	12.953	11.473	9.914	8.026				
26.274	25.978	25.445	24.713	23.806	22.753	21.582	20.321	18.998	17.635	16.251	14.859	13.468	12.074	10.665	9.191	7.420			
26.511	26.223	25.697	24.970	24.070	23.025	21.863	20.614	19.305	17.960	16.599	15.237	13.884	12.545	11.216	9.882	8.497	6.843		
26.715	26.433	25.913	25.192	24.298	23.259	22.105	20.865	19.567	18.235	16.891	15.550	14.226	12.923	11.645	10.387	9.131	7.835	6.296	
26.890	26.614	26.099	25.382	24.493	23.459	22.311	21.079	19.789	18.469	17.138	15.813	14.509	13.232	11.989	10.777	9.592	8.416	7.208	5.781

Table 2. Type A rosette, ASTM E837–13a, $D = 0.202$ in., $G_L = 0.062$ in., $G_W = 0.062$ in., $D_0 = 0.08$ in., $\Delta Z = 0.002$ in.

Matrix $\bar{\mathbf{a}}$ coefficients ($\times 10^3$)

6.967																			
8.366	7.477																		
9.542	8.813	7.676																	
10.580	9.874	8.995	7.658																
11.500	10.796	9.983	8.961	7.475															
12.314	11.605	10.817	9.890	8.754	7.167														
13.030	12.315	11.538	10.654	9.630	8.412	6.766													
13.659	12.936	12.163	11.302	10.332	9.235	7.967	6.301												
14.207	13.479	12.705	11.856	10.917	9.882	8.739	7.450	5.795											
14.683	13.950	13.175	12.332	11.412	10.411	9.333	8.169	6.885	5.268										
15.096	14.358	13.581	12.741	11.832	10.853	9.813	8.714	7.553	6.296	4.737									
15.453	14.710	13.931	13.093	12.189	11.225	10.208	9.148	8.051	6.913	5.699	4.215								
15.760	15.014	14.232	13.394	12.494	11.539	10.537	9.502	8.444	7.367	6.267	5.110	3.711							
16.025	15.275	14.490	13.652	12.754	11.804	10.813	9.795	8.761	7.722	6.680	5.630	4.539	3.231						
16.252	15.499	14.712	13.872	12.976	12.030	11.046	10.038	9.021	8.005	6.999	6.004	5.013	3.993	2.781					
16.447	15.691	14.902	14.061	13.165	12.221	11.241	10.241	9.235	8.236	7.253	6.291	5.352	4.424	3.479	2.362				
16.614	15.856	15.065	14.222	13.326	12.383	11.407	10.412	9.413	8.425	7.457	6.517	5.609	4.730	3.870	3.000	1.977			
16.757	15.997	15.204	14.360	13.463	12.521	11.546	10.555	9.562	8.581	7.624	6.699	5.810	4.960	4.144	3.352	2.557	1.625		
16.879	16.117	15.322	14.477	13.580	12.638	11.664	10.675	9.686	8.710	7.761	6.846	5.971	5.139	4.349	3.598	2.874	2.151	1.306	
16.984	16.220	15.424	14.578	13.680	12.737	11.764	10.777	9.790	8.818	7.874	6.966	6.100	5.281	4.508	3.781	3.093	2.435	1.781	1.019

Matrix $\bar{\mathbf{b}}$ coefficients ($\times 10^3$)

12.869																			
14.858	13.887																		
16.554	15.880	14.456																	
18.082	17.493	16.492	14.706																
19.463	18.920	18.055	16.772	14.704															
20.707	20.197	19.404	18.290	16.776	14.497														
21.821	21.338	20.591	19.569	18.245	16.552	14.128													
22.814	22.354	21.640	20.674	19.454	17.964	16.143	13.633												
23.692	23.253	22.565	21.639	20.483	19.104	17.491	15.588	13.044											
24.465	24.046	23.377	22.481	21.370	20.060	18.561	16.868	14.926	12.392										
25.143	24.740	24.089	23.215	22.136	20.874	19.447	17.868	16.133	14.187	11.699									
25.733	25.347	24.711	23.854	22.800	21.571	20.193	18.686	17.064	15.319	13.400	10.985								
26.246	25.874	25.251	24.409	23.373	22.170	20.827	19.369	17.818	16.183	14.457	12.587	10.267							
26.691	26.331	25.719	24.890	23.869	22.685	21.368	19.945	18.442	16.876	15.256	13.571	11.768	9.558						
27.074	26.726	26.124	25.305	24.296	23.128	21.830	20.433	18.964	17.445	15.891	14.306	12.679	10.957	8.866					
27.405	27.067	26.473	25.663	24.664	23.508	22.225	20.848	19.404	17.918	16.409	14.887	13.355	11.798	10.165	8.199				
27.689	27.360	26.774	25.971	24.981	23.834	22.563	21.201	19.776	18.315	16.837	15.358	13.885	12.418	10.939	9.401	7.561			
27.933	27.611	27.032	26.236	25.252	24.113	22.852	21.502	20.092	18.648	17.194	15.746	14.313	12.901	11.506	10.111	8.669	6.956		
28.142	27.827	27.254	26.463	25.485	24.353	23.100	21.758	20.359	18.930	17.494	16.067	14.663	13.288	11.945	10.628	9.319	7.974	6.385	
28.321	28.012	27.443	26.657	25.684	24.558	23.311	21.977	20.587	19.169	17.746	16.335	14.952	13.604	12.296	11.027	9.790	8.568	7.318	5.848

Table 3. Type B rosette, ASTM E837–13a, $D = 5.13$ mm, $G_L = 1.59$ mm, $G_W = 1.14$ mm, $D_0 = 2.0$ mm, $\Delta Z = 0.05$ mm.

Matrix $\bar{\mathbf{a}}$ coefficients ($\times 10^3$)

7.017																			
8.423	7.531																		
9.605	8.874	7.734																	
10.649	9.941	9.059	7.718																
11.574	10.868	10.053	9.029	7.538															
12.392	11.681	10.893	9.964	8.825	7.233														
13.112	12.395	11.618	10.733	9.706	8.486	6.834													
13.744	13.021	12.247	11.385	10.414	9.315	8.044	6.370												
14.296	13.567	12.793	11.943	11.003	9.966	8.821	7.528	5.865											
14.776	14.041	13.266	12.423	11.501	10.500	9.420	8.253	6.964	5.339										
15.192	14.453	13.675	12.835	11.925	10.946	9.904	8.803	7.638	6.375	4.808									
15.551	14.808	14.028	13.190	12.286	11.321	10.303	9.241	8.141	6.998	5.779	4.285								
15.861	15.114	14.332	13.494	12.594	11.638	10.636	9.599	8.538	7.458	6.353	5.189	3.780							
16.128	15.378	14.593	13.754	12.857	11.906	10.915	9.895	8.859	7.816	6.771	5.715	4.617	3.299						
16.357	15.604	14.817	13.977	13.081	12.134	11.150	10.141	9.122	8.103	7.094	6.095	5.098	4.071	2.848					
16.554	15.798	15.009	14.168	13.272	12.328	11.348	10.347	9.339	8.337	7.351	6.386	5.441	4.508	3.556	2.427				
16.723	15.965	15.173	14.331	13.435	12.492	11.515	10.519	9.519	8.529	7.558	6.615	5.702	4.818	3.952	3.075	2.040			
16.867	16.107	15.314	14.471	13.574	12.632	11.657	10.665	9.670	8.687	7.728	6.799	5.907	5.052	4.231	3.433	2.630	1.687		
16.992	16.229	15.435	14.590	13.693	12.751	11.777	10.787	9.796	8.819	7.867	6.949	6.070	5.234	4.440	3.683	2.952	2.221	1.365	
17.098	16.334	15.538	14.692	13.794	12.852	11.879	10.890	9.902	8.929	7.982	7.071	6.202	5.378	4.601	3.869	3.176	2.510	1.848	1.076

Matrix $\bar{\mathbf{b}}$ coefficients ($\times 10^3$)

13.445																			
15.532	14.529																		
17.313	16.622	15.144																	
18.920	18.318	17.285	15.427																
20.374	19.822	18.931	17.602	15.445															
21.687	21.169	20.354	19.203	17.631	15.250														
22.864	22.374	21.608	20.554	19.182	17.420	14.883													
23.914	23.449	22.718	21.724	20.461	18.913	17.014	14.384												
24.845	24.402	23.698	22.745	21.552	20.121	18.443	16.456	13.786											
25.665	25.243	24.561	23.639	22.493	21.136	19.579	17.814	15.782	13.118										
26.386	25.982	25.318	24.420	23.308	22.002	20.521	18.878	17.066	15.027	12.407									
27.015	26.628	25.980	25.102	24.015	22.745	21.316	19.750	18.058	16.234	14.219	11.672								
27.563	27.191	26.557	25.694	24.628	23.385	21.993	20.479	18.863	17.156	15.348	13.383	10.931							
28.038	27.680	27.058	26.208	25.158	23.936	22.572	21.095	19.531	17.897	16.203	14.435	12.537	10.198						
28.450	28.103	27.492	26.653	25.616	24.410	23.067	21.618	20.091	18.508	16.884	15.224	13.514	11.698	9.481					
28.805	28.470	27.867	27.038	26.012	24.819	23.492	22.064	20.564	19.016	17.441	15.848	14.241	12.602	10.878	8.789				
29.111	28.785	28.191	27.370	26.353	25.170	23.857	22.445	20.965	19.444	17.902	16.356	14.812	13.270	11.712	10.084	8.126			
29.375	29.057	28.470	27.656	26.646	25.473	24.169	22.770	21.306	19.804	18.288	16.775	15.274	13.792	12.324	10.851	9.323	7.496		
29.601	29.291	28.711	27.902	26.899	25.732	24.437	23.048	21.596	20.110	18.613	17.123	15.654	14.212	12.800	11.412	10.028	8.599	6.901	
29.795	29.492	28.917	28.114	27.115	25.955	24.667	23.286	21.844	20.369	18.887	17.415	15.968	14.556	13.182	11.846	10.540	9.245	7.915	6.341

Table 4. Type B rosette, ASTM E837–13a, $D = 0.202$ in., $G_L = 0.062$ in., $G_W = 0.045$ in., $D_0 = 0.08$ in., $\Delta Z = 0.002$ in.

Matrix $\bar{\mathbf{a}}$ coefficients ($\times 10^3$)

7.373																			
8.861	7.910																		
10.111	9.330	8.114																	
11.215	10.459	9.515	8.085																
12.193	11.437	10.564	9.468	7.879															
13.057	12.296	11.449	10.453	9.236	7.540														
13.817	13.048	12.213	11.262	10.162	8.859	7.103													
14.482	13.706	12.874	11.947	10.905	9.728	8.373	6.600												
15.062	14.279	13.446	12.532	11.522	10.410	9.186	7.812	6.054											
15.565	14.776	13.942	13.034	12.043	10.968	9.812	8.568	7.202	5.490										
16.000	15.205	14.369	13.464	12.484	11.432	10.315	9.141	7.903	6.569	4.923									
16.375	15.576	14.736	13.833	12.859	11.821	10.730	9.596	8.426	7.215	5.931	4.368								
16.697	15.894	15.052	14.148	13.179	12.150	11.075	9.966	8.836	7.691	6.525	5.304	3.834							
16.974	16.167	15.322	14.418	13.450	12.428	11.363	10.271	9.167	8.060	6.956	5.846	4.698	3.329						
17.211	16.401	15.554	14.648	13.682	12.663	11.605	10.525	9.437	8.356	7.288	6.236	5.192	4.123	2.856					
17.414	16.601	15.751	14.845	13.878	12.862	11.809	10.736	9.660	8.595	7.551	6.534	5.544	4.571	3.582	2.418				
17.588	16.773	15.920	15.012	14.046	13.030	11.980	10.913	9.845	8.792	7.764	6.769	5.811	4.887	3.987	3.080	2.017			
17.737	16.919	16.065	15.155	14.188	13.173	12.125	11.061	9.999	8.953	7.936	6.957	6.019	5.125	4.271	3.445	2.617	1.651		
17.864	17.044	16.188	15.277	14.309	13.294	12.247	11.186	10.127	9.087	8.078	7.108	6.185	5.310	4.483	3.698	2.945	2.194	1.321	
17.973	17.151	16.293	15.381	14.412	13.397	12.351	11.291	10.235	9.199	8.194	7.232	6.319	5.456	4.647	3.887	3.171	2.487	1.810	1.024

Matrix $\bar{\mathbf{b}}$ coefficients ($\times 10^3$)

14.079																			
16.285	15.213																		
18.169	17.426	15.847																	
19.867	19.218	18.109	16.123																
21.403	20.805	19.846	18.420	16.117															
22.786	22.225	21.346	20.107	18.421	15.883														
24.025	23.493	22.665	21.527	20.052	18.167	15.468													
25.128	24.621	23.829	22.754	21.394	19.734	17.707	14.915												
26.103	25.620	24.855	23.824	22.536	20.998	19.202	17.086	14.261											
26.960	26.498	25.756	24.758	23.519	22.058	20.388	18.504	16.347	13.536										
27.710	27.268	26.545	25.571	24.368	22.959	21.369	19.612	17.684	15.526	12.770									
28.364	27.939	27.233	26.278	25.102	23.731	22.194	20.517	18.715	16.780	14.654	11.983								
28.932	28.523	27.830	26.892	25.736	24.393	22.895	21.272	19.548	17.735	15.824	13.757	11.195							
29.423	29.028	28.348	27.423	26.284	24.962	23.493	21.909	20.237	18.500	16.706	14.844	12.855	10.417						
29.847	29.464	28.796	27.882	26.756	25.451	24.003	22.447	20.814	19.129	17.408	15.657	13.862	11.965	9.661					
30.212	29.841	29.181	28.278	27.162	25.871	24.440	22.905	21.300	19.651	17.980	16.298	14.608	12.894	11.098	8.934				
30.526	30.164	29.513	28.618	27.512	26.231	24.813	23.295	21.711	20.089	18.453	16.818	15.194	13.578	11.952	10.262	8.240			
30.795	30.442	29.799	28.910	27.812	26.540	25.132	23.627	22.059	20.457	18.847	17.246	15.666	14.111	12.578	11.047	9.465	7.583		
31.026	30.680	30.043	29.161	28.069	26.804	25.405	23.911	22.355	20.769	19.177	17.601	16.052	14.539	13.063	11.618	10.183	8.709	6.964	
31.224	30.885	30.253	29.376	28.289	27.031	25.639	24.152	22.606	21.032	19.456	17.897	16.372	14.888	13.451	12.059	10.704	9.366	7.997	6.384

Table 5. Type A rosette, ASTM E837–13a, $D = 5.13$ mm, $G_{\mathrm{L}} = 1.59$ mm, $G_{\mathrm{W}} = 1.59$ mm, $D_0 = 2.0$ mm, $\Delta Z = 0.05$ mm, coefficients of the derivative matrix $\bar{\alpha}_{\mathrm{e1}}$.

| | | |